Research Square

Preprints are preliminary reports that have not undergone peer review. They should not be considered conclusive, used to inform clinical practice, or referenced by the media as validated information.

Experimental zero-added-loss multiplexing Bell-pair source for long-haul quantum networks

Yoshiaki Tsujimoto

tsujimoto@nict.go.jp

National institute of information and communications technology https://orcid.org/0000-0002-7877-3797

Daiki Ichii

Keio university

Rikizo Ikuta

Osaka university https://orcid.org/0000-0001-8628-7177

Mikio Fujiwara

National Institute of Information and Communications Technology

Masahiro Takeoka

Keio University https://orcid.org/0000-0002-4652-4999

Go Kato

National institute of information and communications technology https://orcid.org/0000-0001-5030-5230

Kentaro Wakui

National institute of information and communications technology https://orcid.org/0009-0002-6460-1676

Article

Keywords:

Posted Date: October 27th, 2026

DOI: https://doi.org/10.21203/rs.3.rs-10740579/v1

License: This work is licensed under a Creative Commons Attribution 4.0 International License. Read Full License

Additional Declarations: There is **NO** Competing Interest.

Experimental zero-added-loss multiplexing Bell-pair source for long-haul quantum networks

Yoshiaki Tsujimoto[1*], Daiki Ichii[1,2], Rikizo Ikuta[3,4], Mikio Fujiwara[1], Masahiro Takeoka[1,2], Go Kato[1], Kentaro Wakui[1]

[1]Advanced ICT Research Institute, National Institute of Information and Communications Technology (NICT), Koganei, Tokyo 184-8795, Japan.
[2]Department of Electronics and Electrical Engineering, Keio University, Yokohama, Kanagawa 223-8522, Japan.
[3]Graduate School of Engineering Science, The University of Osaka, Toyonaka, Osaka 560-8531, Japan.
[4]Center for Quantum Information and Quantum Biology, The University of Osaka, Toyonaka, Osaka 560-0043, Japan.

*Corresponding author(s). E-mail(s): tsujimoto@nict.go.jp;

Abstract

Boosting the communication rate of quantum networks is a central challenge in quantum information science. Recently, an efficient entanglement distribution scheme employing quasi-deterministic Bell-pair sources based on time-frequency multiplexing, referred to as zero-added-loss multiplexing (ZALM), has been proposed. Its implementation, however, requires high-fidelity entanglement swapping across densely multiplexed time-frequency modes, which has remained an experimental challenge. Here we demonstrate entanglement swapping across 16 parallel frequency modes with a high average fidelity of $93.9 \pm 1.4\,\%$. Notably, polarization-entangled photon pairs in each frequency mode are spectrally single-mode using only off-the-shelf 50-GHz dense wavelength-division multiplexing (DWDM) filters, eliminating the need for additional narrowband filtering. Furthermore, in order to fully exploit the temporal degree of freedom, the pump pulse is operated with a repetition frequency of 3.0 GHz. By combining the frequency and time multiplexing, the total swapping rate reaches $5.38 \pm 0.17\,\mathrm{pairs\,s^{-1}}$, which corresponds to the ZALM Bell-pair rate of $8.2 \times 10^2\,\mathrm{pairs\,s^{-1}}$. Our results establish the key experimental capabilities required for ZALM and demonstrate a scalable route toward practical high-rate quantum repeaters and long-haul quantum networks.

INTRODUCTION

The realization of quantum networks is a central goal of quantum information science, with applications ranging from secure communication [1] to distributed quantum computation [2] and sensing [3, 4]. In order to achieve both high rates and high fidelity, one promising route is to exploit multiple modes in various photonic degrees of freedom, including frequency [5–8], spatial modes [9], and orbital angular momentum [10, 11] for multiplexed quantum communication. In particular, frequency multiplexing is highly attractive due to its compatibility with existing fiber-based telecommunication infrastructure based on dense wavelength division multiplexing (DWDM) technology and its ability to harness the intrinsically broad spectral bandwidth of photon pairs generated via spontaneous parametric down-conversion (SPDC) [5–8, 12, 13].

Recently, an efficient entanglement distribution scheme was proposed that exploits frequency multiplexing using the broad spectral bandwidth of the SPDC photon pairs, which is called zero-added-loss multiplexing (ZALM) [14]. In the ZALM architecture, a quantum transmitter (QTX) is placed at the central node, and Bell pairs are distributed to neighboring nodes equipped with quantum mode converters and quantum memories, as shown in Fig. 1a. This configuration is known as a midpoint-source configuration and enables a high-rate entanglement distribution with a limited number of quantum memories compared to other architectures, such as the meet-in-the-middle configuration [15]. The QTX employs a ZALM Bell-pair source based on local frequency-multiplexed entanglement swapping [16] to achieve quasi-deterministic entanglement generation, thereby circumventing the switching losses that have rendered previous multiplexing schemes inefficient [17, 18]. Using classical information from the QTX identifying the frequency mode in which the heralding event occurred, the generated photon pairs are converted into the desired time-frequency mode by mode converters at the quantum receivers.

A key advantage of ZALM is that it leverages not only frequency multiplexing but also the ultrafast photon-pair generation capability of SPDC [13], enabling Bell-pair generation with both high probability and high repetition rate. In fact, the ZALM proposal [14] typically requires a DWDM channel bandwidth of 12.5 GHz, a SPDC spectral bandwidth of 10 THz, and a pump repetition rate of 30 GHz to realize dense time-frequency multiplexing. Previous experimental demonstrations of frequency multiplexing have been limited to the direct distribution of entangled photon pairs [5–8]. Frequency multiplexing has also been explored for entanglement swapping between time-frequency entangled photons [19] and quantum fusion of independent quantum networks [20]. However, the wavelengths [19] and architectures [20] demonstrated in these studies, combined with their repetition rates in the tens of MHz range, made it difficult to apply them to the ZALM architecture, particularly with its goal of increasing the entanglement-swapping rate through time-frequency multiplexing.

Here, we demonstrate the ZALM Bell-pair source through high-fidelity entanglement swapping across 16 parallel frequency modes in the telecom C-band for long-haul communication, at a GHz-level repetition rate. To enable direct frequency multiplexing with off-the-shelf 50-GHz DWDM filters, we combine pump-pulse waveshaping with careful selection of the SPDC crystal length such that each frequency channel is spectrally single-mode, leading to an average Hong-Ou-Mandel (HOM) interference [21]

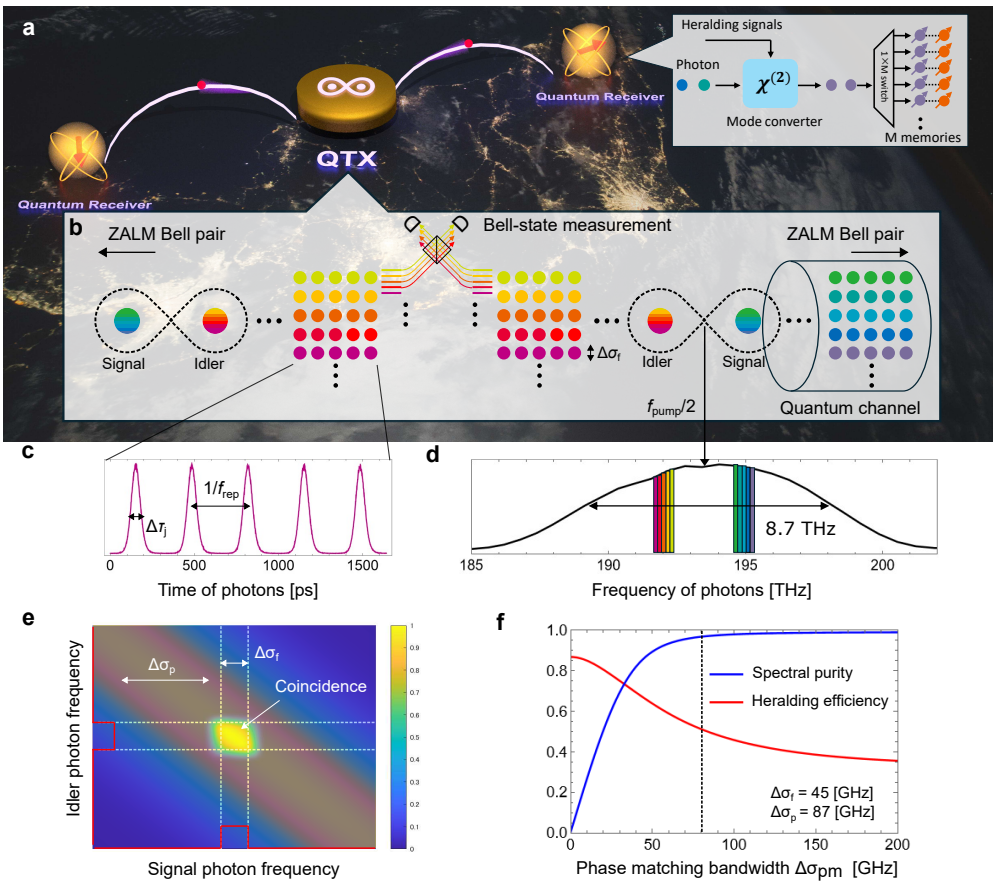

Fig. 1 ZALM architecture based on time-frequency-multiplexed entanglement swapping. a Concept of the entanglement distribution using ZALM. Background image adapted from an image courtesy of the Earth Science and Remote Sensing Unit, NASA Johnson Space Center (ISS053-E-209380). **b** Implementation of the QTX using time-frequency-multiplexed entanglement swapping based on SPDC. **c** The temporal distribution of the photon counts. The repetition frequency and the timing jitter of the photon detector are $f_{\mathrm{rep}} = 3.0\,\mathrm{GHz}$ and $\Delta\tau_{\mathrm{j}} = 39\,\mathrm{ps}$, respectively. **d** The spectrum of the SPDC photons. The center frequency is chosen to be $f_{\mathrm{pump}}/2 = 193.4\,\mathrm{THz}$. **e** The joint spectral amplitude of the photon pair in a single DWDM channel. We focus on a pair of output modes of the DWDM filters in the signal and idler arms. **f** The relation among the phase-matching bandwidth, spectral purity and heralding efficiency of the swapped photon pair under the condition of $\Delta\sigma_{\mathrm{f}} = 45\,\mathrm{GHz}$ and $\Delta\sigma_{\mathrm{p}} = 87\,\mathrm{GHz}$. The black dotted line shows the experimental phase-matching bandwidth of $\Delta\sigma_{\mathrm{pm}} = 80\,\mathrm{GHz}$.

visibility of 95.0±0.7 % across all 16 modes. In addition to frequency multiplexing, we fully exploit the temporal degree of freedom by operating the pump laser at a repetition rate of 3.0 GHz [13, 22]. This record-high repetition rate allows us to increase the generation rate of the SPDC photon pairs without compromising the interference visibility of the photons. By jointly exploiting the frequency and temporal degrees of freedom, we achieve a total swapping rate of 5.38±0.17 pairs s^{-1} and an average entanglement

fidelity of 93.9±1.4 %, which corresponds to the ZALM Bell-pair rate of 8.2×10^2 pairs s^{-1}. These results establish a new performance regime for photonic entanglement swapping beyond those accessed in previous experiments. Moreover, simulations based on experimental parameters show that, by fully exploiting the 8.7-THz SPDC spectrum, the ZALM Bell-pair rate can reach 10^5 pairs s^{-1} while maintaining an entanglement fidelity of 91 %. Our results establish dense time-frequency-multiplexed entanglement swapping as a viable route toward high-rate quantum communication and constitute a key enabling step toward the ZALM architecture for long-haul quantum networks.

RESULTS

Experimental challenges for ZALM Bell-pair source

In this work, we focus on the QTX shown in Fig. 1b and address the key experimental challenges in realizing ZALM Bell-pair source. At each SPDC source, the lower-frequency (idler) and higher-frequency (signal) components of the SPDC photon pair are spatially separated, and the pairs that satisfy energy conservation are entangled in polarization degree of freedom. The idler photons are interfered on a 50:50 beamsplitter (BS) to perform a time-frequency-resolved Bell-state measurement (BSM), thereby allowing time-frequency-multiplexed entanglement swapping. Under the condition that coincidence events between idler photons of the same frequency are detected at the BSM node, a quasi-deterministic generation of entangled photon pairs becomes possible when the number of frequency modes is sufficiently large [14]. A key challenge in QTX is to maximize the number of modes in the available time-frequency space. However, compared with simple transmission of entangled photon pairs, entanglement swapping imposes more stringent constraints on time-frequency-mode multiplexing.

For the temporal degree of freedom, the number of temporal modes is increased by increasing the pump repetition rate f_{rep} as shown in Fig. 1c. However, when the pulse spacing becomes shorter than the timing jitter of the photon detectors $\Delta\tau_{\mathrm{j}}$, photons from neighboring pulses can enter the coincidence detection window. We emphasize that this effect is much more pronounced than in the case of a direct distribution of entangled photon pairs. In the direct distribution, even under the conditions described above, the main consequence is merely a small admixture of error events due to multiphoton generation [13]. In contrast, in entanglement swapping, insufficient temporal resolution of the pulse train directly results in an increase in the number of modes contributing to the HOM interference, which dramatically degrades the interference visibility [22]. Thus, a time-resolved detection of the pulse train satisfying the condition $1/f_{\mathrm{rep}} \gg \Delta\tau_{\mathrm{j}}$ is necessary.

For frequency multiplexing, the accessible bandwidth is limited by the phase-matching bandwidth of the nonlinear optical crystal for SPDC, within which a higher multiplexing density enables the utilization of a larger number of frequency modes as shown in Fig. 1d. Here, an important trade-off exists between the spectral bandwidth of the pump pulses and that of each multiplexed mode. For each frequency mode that can be separated in parallel by the DWDM filters, spectral purity is guaranteed as long as the spectral bandwidth of the pump pulses $\Delta\sigma_{\mathrm{p}}$ is sufficiently larger than the filter bandwidth $\Delta\sigma_{\mathrm{f}}$ [23, 24] as shown in Fig. 1e. However, if $\Delta\sigma_{\mathrm{p}}$ is excessively larger

than $\Delta\sigma_{\mathrm{f}}$, the following two detrimental effects occur. The first issue is inter-channel cross talk of DWDM filters. Unlike the case of continuous-wave pumping, where strong frequency-correlation is imposed by energy conservation, the finite bandwidth of the pump pulses allows photon pairs to leak into adjacent frequency modes. The second issue is a photon loss. When the spectrally pure mode is further subdivided, it effectively results in a photon loss even if the filter transmittance is 100 % [25]. Consequently, it is necessary to tune the pump bandwidth so as to achieve the required spectral purity while minimizing the photon loss as well as the inter-channel crosstalk.

In this work, we employ type-0 periodically poled lithium niobate waveguides (PPLN/Ws) for the SPDC, which provide a broad phase-matching bandwidth. The experimentally measured spectrum of the generated photon pairs is shown in Fig. 1d, exhibiting a bandwidth of 8.7 THz FWHM. Using standard 50-GHz DWDM filters, we implement frequency multiplexing over 16 frequency modes in each of the signal and idler modes. It should be noted that these 16 DWDM output channels merely conform to the standard specifications of a single commercially available device, and it is easy to increase the number of channels further. The experimental parameters are optimized to satisfy the constraints as follows. First, the SPDC sources were operated at a repetition frequency of $f_{\mathrm{rep}} = 3.0\,\mathrm{GHz}$, which remains fully resolvable with our superconducting single-photon detectors (SSPDs) with an average timing jitter of $\Delta\tau_{\mathrm{j}} = 39\,\mathrm{ps}$ as shown in Fig. 1c. Second, the joint spectral amplitude (JSA) was engineered to simultaneously achieve high spectral purity and high heralding efficiency. In our experiment, not only $\Delta\sigma_{\mathrm{p}}$ but also the phase-matching bandwidth $\Delta\sigma_{\mathrm{pm}}$ of the PPLN/W for SPDC contributes to the trade-off between spectral purity and photon transmittance. Thus, after maximizing $\Delta\sigma_{\mathrm{p}}$, we selected an appropriate PPLN/W length corresponding to the desired $\Delta\sigma_{\mathrm{pm}}$. Fig. 1f shows the relationship between the spectral purity and the heralding efficiency (transmittance) of the photon pair as a function of $\Delta\sigma_{\mathrm{pm}}$, while keeping $\Delta\sigma_{\mathrm{f}}$ and $\Delta\sigma_{\mathrm{p}}$ fixed (see Methods for details). The simulation shows that $\Delta\sigma_{\mathrm{pm}}$ corresponding to a 2.0 cm-long PPLN/W simultaneously provides a spectral purity of 97 % and a heralding efficiency of 57 %.

Experimental setup

The experimental setup for time-frequency-multiplexed entanglement swapping is shown in Fig. 2. We prepare pump pulses with f_{rep} =3.0 GHz by doubling the frequency of the fundamental telecom pulses via second harmonic generation (SHG) using a 1.0-cm-long type-0 PPLN/W. The center frequency of the fundamental pulse is chosen as 193.4 THz, which corresponds to Ch.34 of the ITU channel. Using a wave shaper, we optimized the bandwidth and dispersion of the fundamental pulse to fully utilize the phase-matching bandwidth of the 1.0-cm-long PPLN/W while minimizing the pulse duration of the SHG pulse. The FWHMs of the SHG pulse in the frequency (time) domain were measured to be 87 GHz (5.0 ps), respectively, assuming sech^2 spectral (temporal) profiles. The time-bandwidth product is calculated as 0.44, which is larger than the transform-limited value of 0.315, indicating a slight deviation from the ideal sech^2 spectral and temporal profiles. The SHG pulses are used to pump entangled photon pair sources (EPSs) I and II. Each EPS consists of a 2.0-cm-long type-0 PPLN/W in a Sagnac interferometer with a dual-wavelength polarizing

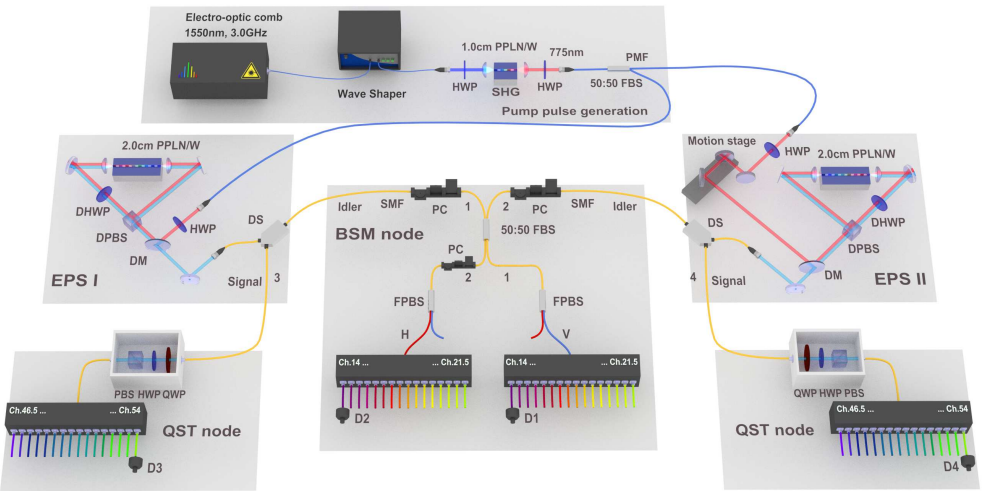

Fig. 2 Experimental setup for time-frequency-multiplexed entanglement swapping. Pump pulses centered at 775 nm with a 3.0-GHz repetition rate is prepared by second harmonic generation (SHG) of the electro-optic comb centered at 1550 nm (193.4 THz). The SHG pulses are used to pump entangled photon pair sources (EPSs) I and II based on PPLN/Ws. The signal and idler photons are separated into the shorter and longer wavelengths with respect to 1550 nm by dichroic separators (DSs) integrated in the fiber pigtail. The signal and idler photons are sent to the quantum state tomography (QST) nodes and Bell state measurement (BSM) node, respectively. After 16 frequency modes in each of signal and idler photons are extracted, photons are detected by SSPDs (D1-D4). The four-fold coincidence counts are recorded by time-to-digital converter (not shown). The details are given in main text. HWP: half waveplate, QWP: quarter waveplate, PBS: polarizing beamsplitter, PMF: polarization maintaining fiber, SMF: single-mode fiber, DHWP: dual-wavelength HWP, DPBS: dual-wavelength PBS, DM: dichroic mirror, PC: polarization controller, 50:50 FBS: 50:50 fiber-based beamsplitter, FPBS: fiber-based PBS.

beamsplitter (DPBS). The phase-matching function of the 2.0-cm-long PPLN/W is well fitted by a super-Gaussian with order 1.4 and a FWHM of $\Delta\sigma_{\rm pm} = 80$ GHz, which is slightly narrower than the pump bandwidth $\Delta\sigma_p$ (see Methods for the fitting function).

The signal and idler wavelengths are spatially separated by fiber-based dichroic separators (DSs). The idler photons are sent to the BSM node to perform the time-frequency-resolved BSM. Polarization rotations during propagating single-mode fibers are compensated by using in-line polarization controllers. After mixing two idler photons by a fiber-based 50:50 beamsplitter, horizontally (H) and vertically (V) polarized components in left and right output modes are respectively extracted using fiber-based PBSs. Then, 16 frequency modes are extracted using 50-GHz DWDM filters (from ITU Ch.14 to Ch.21.5) followed by photon detection by SSPDs (D1 and D2). The measured transmission spectrum of the flat-top DWDM filters is well fitted by a super-Gaussian with order 2.5 and a FWHM of $\Delta\sigma_{\rm f}$ =45 GHz. The average timing jitter per channel is 39 ps, including the jitter of a time-to-digital converter (TDC), which is much smaller than the pulse interval of $1/f_{\rm rep}$ =333 ps allowing time-resolved measurements. The signal photons are sent to the quantum state tomography (QST) nodes to perform

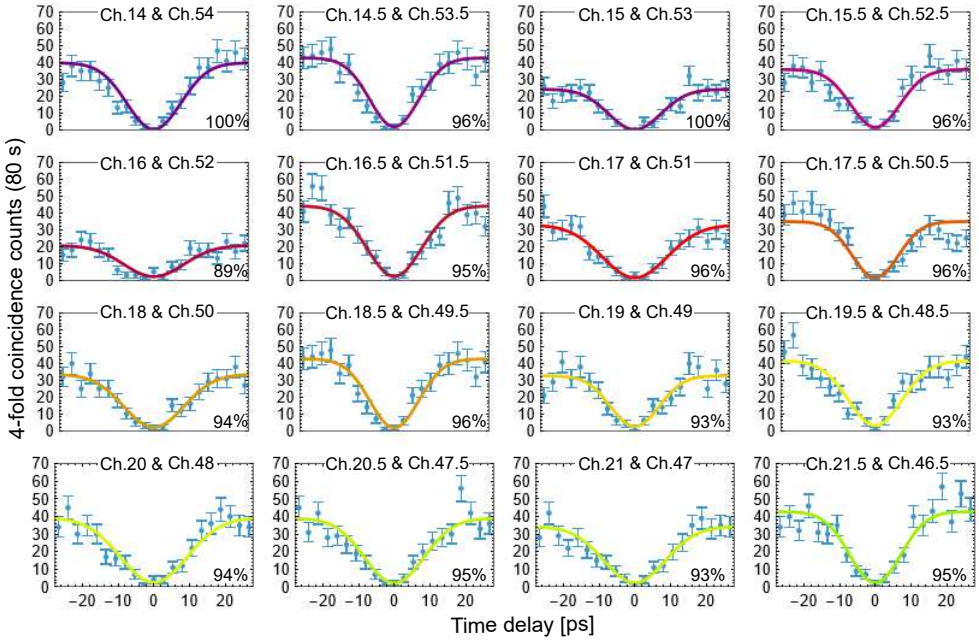

Fig. 3 Frequency-multiplexed HOM dips. The HOM dips and visibilities for 16 frequency modes in parallel. Each frequency-mode pair is denoted as Ch.n_i & Ch.n_s, where Ch.n_i (Ch.n_s) represents the ITU channel of the idler (signal) photon, respectively. The measurement time was 80 s for each point. The error bars correspond to the standard deviations with the assumption of Poisson statistics for the photon counts. The solid curves are the maximum-likelihood fits using a Gaussian dip model assuming Poisson counting statistics.

polarization measurements on the swapped state. The polarization rotation in each arm is canceled by rotating a pair of a quarter waveplate and half waveplate (not shown). After performing polarization projections, corresponding 16 frequency modes are extracted using 50 GHz DWDM filters (from ITU Ch.46.5 to Ch.54) followed by photon detection by SSPDs (D3 and D4).

Frequency-multiplexed HOM interference

To assess the indistinguishability of the heralded idler photons in each ITU channel, the HOM interference experiment was performed. In this experiment, the four-fold coincidence events of H-polarized components were recorded by a TDC with changing the relative delay of two idler photons using a motion stage placed at EPS Ⅱ in Fig. 2. In postprocessing, we apply coincidence windows to the detection signals from D2, D3, and D4, conditioned on a detection event at D1. The width of each coincidence window, τ_w, was chosen to be 100 ps such that $\Delta\tau_\mathrm{d} < \tau_\mathrm{w} < 1/f_\mathrm{rep}$, where $\Delta\tau_\mathrm{d}$ is the temporal width of the coincidence peak given by $\Delta\tau_\mathrm{d} = \sqrt{2\Delta\tau_\mathrm{j}^2 + T_\mathrm{c}^2} = 57\,\mathrm{ps}$, with $\Delta\tau_\mathrm{j}$ =39 ps being the detector timing jitter and $T_\mathrm{c} = 15\,\mathrm{ps}$ the photon coherence time. The repetition period was $1/f_\mathrm{rep} = 333\,\mathrm{ps}$. The observed HOM dips for 16 ITU channel

combinations (from ITU Ch.14 & Ch.54 to Ch.21.5 & Ch.46.5) are shown in Fig. 3. The HOM visibilities were obtained by fitting the measured coincidence counts to the model using maximum-likelihood estimation assuming Poisson counting statistics. The average visibility is 95.0±0.7 %, indicating that the heralded idler photons in each mode present a nearly perfect indistinguishability. The experimentally obtained values can be evaluated using the following formula [22, 26]

$$V_{\mathrm{th}} = \frac{P}{1 + \frac{\zeta g_{\mathrm{I}}^{(2)} + \zeta^{-1} g_{\mathrm{II}}^{(2)}}{2}}, \tag{1}$$

where P is the spectral purity of the photon pair, assuming identical Schmidt-mode structures for the two input photons, ζ is the intensity ratio of the heralded idler photons from EPS I and EPS II, and $g_{\mathrm{I}}^{(2)}$ and $g_{\mathrm{II}}^{(2)}$ are the corresponding intensity correlation functions. Using the experimental values of ITU Ch.21.5 & Ch.46.5 as $\zeta = 1.0$, $g_{\mathrm{I}}^{(2)} = 2.8 \times 10^{-2}$ and $g_{\mathrm{II}}^{(2)} = 3.5 \times 10^{-2}$, and P =97 % estimated by the simulation, V_{th} is calculated as 94 %, which is in reasonable agreement with the experimental value.

Generation of ZALM Bell-pairs

We first characterize the initial quantum states generated by EPS I and EPS II. As a specific example, we present experimental results for the case where the idler and signal photon frequencies correspond to ITU Ch.21.5 & Ch.46.5, respectively. The average photon numbers of the photon pairs are estimated to be 3.3×10^{-3} for EPS I and 4.6×10^{-3} for EPS II, respectively. The density operators of the initial states ρ_{13} and ρ_{24}, generated by EPS I and EPS II, respectively, are reconstructed by performing QST as shown in Figs. 4a and b, respectively. In our setup, since the relative phases between the H and V polarizations in the initial states are not adjusted, the initial states correspond to the Bell state $|\Phi^+\rangle := (|HH\rangle + |VV\rangle)/\sqrt{2}$ with its phase rotated by a local unitary operation as $R(\phi)|\Phi^+\rangle$, where $|H(V)\rangle$ represents the horizontally (vertically) polarized single-photon state and $R(\phi) := |H\rangle\langle H| + e^{i\phi}|V\rangle\langle V|$. The fidelity to the maximally entangled state is defined by $F_{\mathrm{in}} := \max_{\phi}\langle\Phi^+|R^\dagger(\phi)\rho R(\phi)|\Phi^+\rangle$, which are estimated to be 98.81±0.03 % and 98.74±0.03 % for ρ_{13} and ρ_{24}, respectively. These values indicate that the nearly ideal initial states are prepared.

The entanglement swapping experiments were performed in parallel across 16 frequency modes. We briefly describe the entanglement-swapping procedure for each frequency mode in the present experiment. When a BSM corresponding to a projection onto $|\Psi^-\rangle := (|HV\rangle - |VH\rangle)/\sqrt{2}$ is performed on the idler photons in modes 1 and 2, the unnormalized state after a successful BSM is given by

$${}_{12}\langle\Psi^-|R_3(\phi_3)|\Phi^+\rangle_{13} \otimes R_4(\phi_4)|\Phi^+\rangle_{24} = \frac{1}{2} R_3(\phi_3) R_3^\dagger(\phi_4)|\Psi^-\rangle_{34}, \tag{2}$$

which is a state obtained from $|\Psi^-\rangle$ by a local unitary phase rotation by an angle $\phi_3 - \phi_4$. In our experiment, the success probability of the BSM is $P_{\mathrm{BSM}} = 1/8$ since only $|VH\rangle_{12}$ is measured at the BSM node. In the experiment, QST is performed on

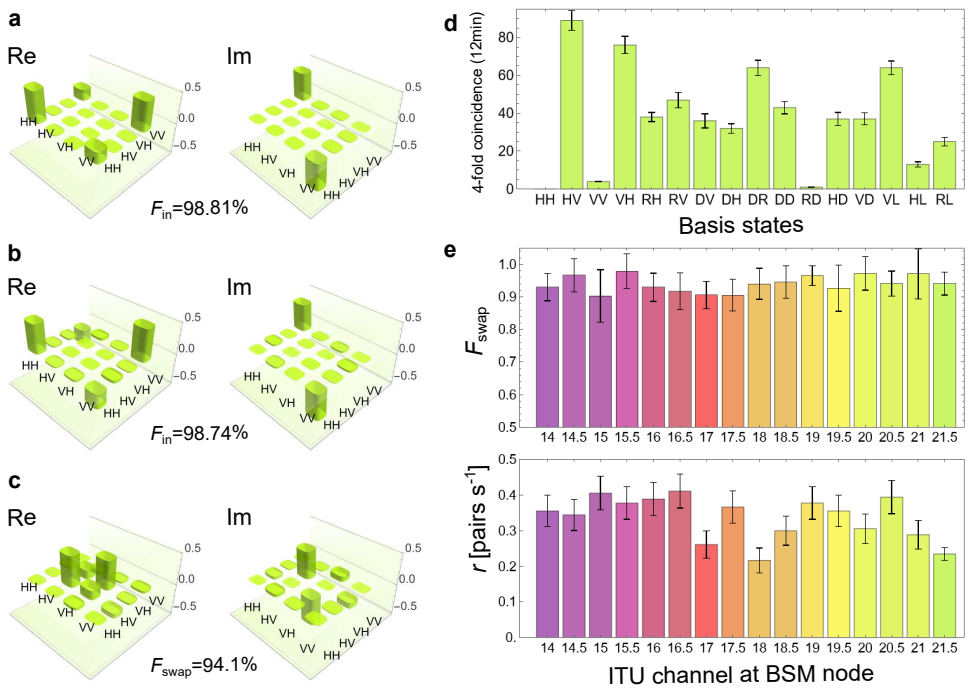

Fig. 4 Results for time-frequency-multiplexed entanglement swapping a,b The reconstructed density matrices of input states. **c** The reconstructed density matrix of the swapped state heralded by the BSM in ITU Ch.21.5. **d** The four-fold coincidence counts for 16 measurement basis states. **e** The fidelities of the swapped states (F_{swap}) and the four-fold coincidence count rates (r) for 16 independent ITU channel combinations. The integration time was 3 min per basis state, except for ITU Ch. 21.5 (12 min per basis state).

the signal photons in modes 3 and 4, conditioned on coincidence detection between D1 and D2. As in the HOM experiment, we set the coincidence windows with τ_{w} =100 ps. The reconstructed density operator of the swapped state ρ_{34} and the four-fold coincidence counts for each measurement basis state are shown in Fig. 4c and d, respectively. The fidelity is $F_{\mathrm{swap}} := \max_{\phi}\langle\Psi^-|R^\dagger(\phi)\rho_{34}R(\phi)|\Psi^-\rangle = 94.1 \pm 3.5\,\%$, indicating that strong entanglement is generated in the swapped state. Maximization over ϕ was performed independently for each frequency mode. The swapping rate r is calculated as $\sum_{i,j\in\{H,V\}} C_{ij}/T_{\mathrm{meas}}$, where C_{ij} denotes the four-fold coincidence count for the polarization basis state $|ij\rangle$ and T_{meas} is the integration time, yielding $r = 0.27$ pairs s^{-1}. The measured values of F_{swap} and r for the 16 ITU channel combinations are summarized in Fig. 4e. The rate-weighted average fidelity of the swapped Bell pairs $F_{\mathrm{exp}} := \sum_k r_k F^{(k)}_{\mathrm{swap}}/\sum_k r_k$, and the total swapping rate, $r_{\mathrm{tot}} := \sum_k r_k$, are measured to be 93.9±1.4 % and 5.38 ± 0.17 pairs s^{-1}, respectively. Here, r_k and $F^{(k)}_{\mathrm{swap}}$ denote the swapping rate and the entanglement fidelity for the kth ITU channel combination, respectively. We estimate the ZALM Bell-pair rate r_{ZALM} by correcting only for the

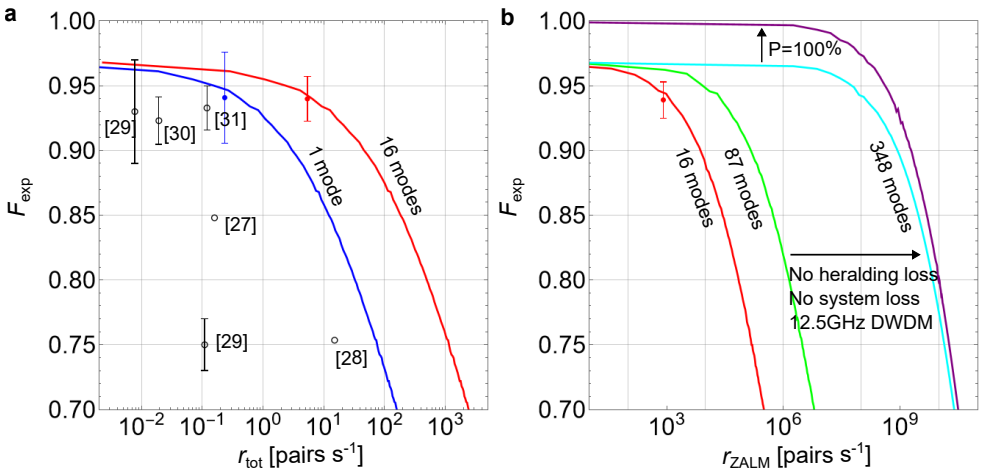

Fig. 5 Simulation results for the rate-fidelity trade-off a The relationship between r_{tot} and F_{exp}. The curves are obtained by the theoretical simulation using experimental parameters. The filled and hollow circles corresponds to our experimental results and previous results [27–31], respectively. **b** The relationship between r_{ZALM} and F_{exp}. The red dot and curve show our experimental result and simulation result with current experimental parameters, respectively. The green curve corresponds to the case of $P_{\mathrm{BSM}} = 1/2$ with frequency multiplexing over the full SPDC bandwidth. The cyan curve shows the simulated performance with improved optical loss and frequency-multiplexing density, while the purple curve further includes an improvement in spectral purity.

detection losses in signal modes 3 and 4, defined as

$$r_{\mathrm{ZALM}} := \sum_{i,j\in\{H,V\}} \frac{C_{ij}}{\eta_{i_3}\eta_{j_4}T_{\mathrm{meas}}}, \tag{3}$$

where η_{H_3}, η_{V_3}, η_{H_4}, and η_{V_4} are 7.4 %, 7.4 %, 8.0 %, and 8.9 %, respectively, yielding $r_{\mathrm{ZALM}} = 8.2\times10^2$ pairs s^{-1}. The intrinsic heralding efficiencies of 57 % due to spectral filtering in each signal modes 3 and 4 are not corrected for, as this filtering is required to achieve the measured spectral purity (see Methods for details).

DISCUSSION

In this section, we clarify the trade-off between r_{tot} and F_{exp} using a theoretical model together with experimental parameters. We further discuss future prospects for increasing r_{ZALM} by improving the key experimental parameters and estimate the achievable performance. We modeled the experimental system using the Gaussian-state characteristic-function method [32–34] and performed numerical simulations using the independently characterized system parameters, including optical loss, spectral purity, and detector quantum efficiency (See Supplementary Note 1 for details). Fig. 5a shows the relationship between the total swapping rate r_{tot} and the rate-weighted average fidelity F_{exp}. The blue and red curves represent the simulated

rate-fidelity trade-offs for the single-mode and 16-frequency-multiplexed cases, respectively, obtained by varying the average photon number of each EPS. The corresponding experimental results are shown by the blue and red solid circles. For comparison, previous demonstrations of entanglement swapping using broadband sources [27–31] are shown as open circles, all of which lie below the simulated single-mode rate-fidelity trade-off for our experimental system. The ultrafast repetition rate of the SPDC source enables this superior single-mode rate-fidelity trade-off. The 16-channel frequency multiplexing further improves the rate-fidelity trade-off, yielding a substantially higher r_{tot} for a given F_{exp}.

Fig. 5b shows the relationship between r_{ZALM} and F_{exp}. The red dot and curve correspond to the experimental value and the simulation curve for 16 frequency multiplexing, respectively. An experimental value of $r_{\mathrm{ZALM}} = 8.2 \times 10^2$ pairs s^{-1} was demonstrated with a rate-weighted average fidelity of $F_{\mathrm{swap}} = 93.9 \pm 1.4\,\%$. The green curve shows the simulated performance achievable without substantial modifications to the experimental setup, in which a BSM capable of discriminating two Bell states ($P_{\mathrm{BSM}} = 1/2$) is implemented and the entire SPDC bandwidth of 8.7 THz is utilized for frequency multiplexing. The experimentally measured SPDC spectrum, fitted to the measured data, is used in the simulation to account for its nonuniform spectral profile, as shown in Fig. 1d. It should be noted that, even at this stage, $r_{\mathrm{ZALM}} = 10^5$ pairs s^{-1} can be achieved while maintaining $F_{\mathrm{exp}} = 91\,\%$.

As shown by the cyan curve in Fig. 5b, reaching the 10^9 pairs s^{-1} regime in r_{ZALM} requires both denser frequency multiplexing and lower system loss. Specifically, a channel spacing of 12.5 GHz, together with substantial reductions in system loss, is assumed, primarily by eliminating the 4.8 dB insertion losses of the DWDM filters in the BSM node and the additional 2.5 dB loss associated with the intrinsic heralding efficiency of 57 % in each signal and idler arm (see Methods for its calculation). Such a reduction in the latter loss could be achieved by using intrinsically spectrally pure photon-pair sources, such as quantum frequency-comb states, via domain-engineering [35] or cavity-enhanced SPDC [36–38]. The purple curve further assumes unity spectral purity ($P = 100\,\%$) in addition to the above improvements. Under these conditions, r_{ZALM} on the order of 10 MHz remains achievable even when requiring $F_{\mathrm{exp}} = 99\,\%$. Compared with the theoretical proposal in Ref. [14], the achievable r_{ZALM} is approximately two orders of magnitude lower for the same repetition rate and F_{exp}. This discrepancy arises from the use of threshold detectors in the BSM. By replacing them with high-speed photon-number-resolving detectors [39–42], which can effectively suppress multi-photon contributions, it would achieve both r_{ZALM} and F_{exp} comparable to those predicted in Ref. [14].

In conclusion, we have demonstrated a ZALM Bell-pair source. Using commercially available 50-GHz DWDM filters, we implemented time-frequency-multiplexed entanglement swapping and successfully achieved the average fidelity of $93.9 \pm 1.4\,\%$ across the 16 ITU channel combinations. By combining frequency multiplexing with high repetition-rate operation, we realized a total swapping rate of 5.38 ± 0.17 pairs s^{-1} corresponding to the ZALM Bell-pair rate of 8.2×10^2 pairs s^{-1}. These results place our experiment in a performance regime that has not been reached by previous experiments. Moreover, our numerical simulations have identified the key challenges

that must be overcome to realize 10^9-rate ZALM Bell-pair generation. Recently, a theoretical proposal suggested exploiting BSM events involving different frequency pairs, enabling the advantage of frequency multiplexing to scale quadratically with the multiplexing factor rather than linearly [43]. Together with such advances in repeater protocols, the experimental techniques demonstrated in this work represent an important step toward the practical realization of high-rate quantum repeaters.

References

[1] Pirandola, S., Andersen, U.L., Banchi, L., Berta, M., Bunandar, D., Colbeck, R., Englund, D., Gehring, T., Lupo, C., Ottaviani, C., Pereira, J.L., Razavi, M., Shaari, J.S., Tomamichel, M., Usenko, V.C., Vallone, G., Villoresi, P., Wallden, P.: Advances in quantum cryptography. Adv. Opt. Photon. **12**(4), 1012–1236 (2020) https://doi.org/10.1364/AOP.361502

[2] Monroe, C., Raussendorf, R., Ruthven, A., Brown, K.R., Maunz, P., Duan, L.-M., Kim, J.: Large-scale modular quantum-computer architecture with atomic memory and photonic interconnects. Phys. Rev. A **89**, 022317 (2014) https://doi.org/10.1103/PhysRevA.89.022317

[3] Zhang, Z., Zhuang, Q.: Distributed quantum sensing. Quantum Science and Technology **6**(4), 043001 (2021) https://doi.org/10.1088/2058-9565/abd4c3

[4] Kómár, P., Kessler, E.M., Bishof, M., Jiang, L., Sørensen, A.S., Ye, J., Lukin, M.D.: A quantum network of clocks. Nature Physics **10**(8), 582–587 (2014) https://doi.org/10.1038/nphys3000

[5] Aktas, D., Fedrici, B., Kaiser, F., Lunghi, T., Labonté, L., Tanzilli, S.: Entanglement distribution over 150 km in wavelength division multiplexed channels for quantum cryptography. Laser & Photonics Reviews **10**(3), 451–457 (2016) https://doi.org/10.1002/lpor.201500258

[6] Wengerowsky, S., Joshi, S.K., Steinlechner, F., Hübel, H., Ursin, R.: An entanglement-based wavelength-multiplexed quantum communication network. Nature **564**(7735), 225–228 (2018) https://doi.org/10.1038/s41586-018-0766-y

[7] Zhuang, S.-C., Li, B., Zheng, M.-Y., Zeng, Y.-X., Wu, H.-N., Li, G.-B., Yao, Q., Xie, X.-P., Li, Y.-H., Qin, H., You, L.-X., Xu, F., Yin, J., Cao, Y., Zhang, Q., Peng, C.-Z., Pan, J.-W.: Ultrabright entanglement based quantum key distribution over a 404 km optical fiber. Phys. Rev. Lett. **134**, 230801 (2025) https://doi.org/10.1103/PhysRevLett.134.230801

[8] Mueller, A., Davis, S.I., Korzh, B., Valivarthi, R., Beyer, A.D., Youssef, R., Sinclair, N., Peña, C., Shaw, M.D., Spiropulu, M.: High-rate multiplexed entanglement source based on time-bin qubits for advanced quantum networks. Optica Quantum **2**(2), 64–71 (2024) https://doi.org/10.1364/OPTICAQ.509335

[9] Ortega, E.A., Fuenzalida, J., Dovzhik, K., Shiozaki, R.F., Alvarado-Zacarias, J.C., Amezcua-Correa, R., Bohmann, M., Wengerowsky, S., Ursin, R.: Implementation of space-division multiplexed entanglement-based quantum cryptography over multicore fiber. Optica Quantum **2**(4), 260–265 (2024) https://doi.org/10.1364/OPTICAQ.527903

[10] Chen, Y., Liu, S., Lou, Y., Jing, J.: Orbital angular momentum multiplexed quantum dense coding. Phys. Rev. Lett. **127**, 093601 (2021) https://doi.org/10.1103/PhysRevLett.127.093601

[11] Liu, S., Lou, Y., Jing, J.: Orbital angular momentum multiplexed deterministic all-optical quantum teleportation. Nature Communications **11**(1), 3875 (2020) https://doi.org/10.1038/s41467-020-17616-4

[12] Ikuta, R., Tani, R., Ishizaki, M., Miki, S., Yabuno, M., Terai, H., Imoto, N., Yamamoto, T.: Frequency-multiplexed photon pairs over 1000 modes from a quadratic nonlinear optical waveguide resonator with a singly resonant configuration. Phys. Rev. Lett. **123**, 193603 (2019) https://doi.org/10.1103/PhysRevLett.123.193603

[13] Wakui, K., Tsujimoto, Y., Fujiwara, M., Morohashi, I., Kishimoto, T., China, F., Yabuno, M., Miki, S., Terai, H., Sasaki, M., Takeoka, M.: Ultra-high-rate nonclassical light source with 50 GHz-repetition-rate mode-locked pump pulses and multiplexed single-photon detectors. Opt. Express **28**(15), 22399–22411 (2020) https://doi.org/10.1364/OE.397030

[14] Chen, K.C., Dhara, P., Heuck, M., Lee, Y., Dai, W., Guha, S., Englund, D.: Zero-added-loss entangled-photon multiplexing for ground- and space-based quantum networks. Phys. Rev. Appl. **19**, 054029 (2023) https://doi.org/10.1103/PhysRevApplied.19.054029

[15] Jones, C., Kim, D., Rakher, M.T., Kwiat, P.G., Ladd, T.D.: Design and analysis of communication protocols for quantum repeater networks. New Journal of Physics **18**(8), 083015 (2016) https://doi.org/10.1088/1367-2630/18/8/083015

[16] Żukowski, M., Zeilinger, A., Horne, M.A., Ekert, A.K.: "event-ready-detectors" bell experiment via entanglement swapping. Phys. Rev. Lett. **71**, 4287–4290 (1993) https://doi.org/10.1103/PhysRevLett.71.4287

[17] Mower, J., Englund, D.: Efficient generation of single and entangled photons on a silicon photonic integrated chip. Phys. Rev. A **84**, 052326 (2011) https://doi.org/10.1103/PhysRevA.84.052326

[18] Dhara, P., Johnson, S.J., Gagatsos, C.N., Kwiat, P.G., Guha, S.: Heralded multiplexed high-efficiency cascaded source of dual-rail entangled photon pairs using spontaneous parametric down-conversion. Phys. Rev. Appl. **17**, 034071 (2022) https://doi.org/10.1103/PhysRevApplied.17.034071

[19] Merkouche, S., Thiel, V., Davis, A.O.C., Smith, B.J.: Heralding multiple photonic pulsed bell pairs via frequency-resolved entanglement swapping. Phys. Rev. Lett. **128**, 063602 (2022) https://doi.org/10.1103/PhysRevLett.128.063602

[20] Huang, Y., Yang, Y., Li, H., Wang, J., Qiu, J., Qi, Z., Zhang, Y., Li, Y., Zheng, Y., Chen, X.: Quantum fusion of independent networks based on multi-user entanglement swapping. Nature Photonics **20**(1), 87–95 (2026) https://doi.org/10.1038/s41566-025-01792-0

[21] Hong, C.K., Ou, Z.Y., Mandel, L.: Measurement of subpicosecond time intervals between two photons by interference. Phys. Rev. Lett. **59**, 2044–2046 (1987) https://doi.org/10.1103/PhysRevLett.59.2044

[22] Tsujimoto, Y., Wakui, K., Fujiwara, M., Sasaki, M., Takeoka, M.: Ultra-fast hong-ou-mandel interferometry via temporal filtering. Opt. Express **29**(23), 37150–37160 (2021) https://doi.org/10.1364/OE.430502

[23] Zukowski, M., Zeilinger, A., Weinfurter, H.: Entangling photons radiated by independent pulsed sources. Annals of the New York academy of Sciences **755**(1), 91–102 (1995) https://doi.org/10.1111/j.1749-6632.1995.tb38959.x

[24] Rarity, J.: Interference of single photons from separate sources. Annals of the New York academy of Sciences **755**(1), 624–631 (1995) https://doi.org/10.1111/j.1749-6632.1995.tb39002.x

[25] Meyer-Scott, E., Montaut, N., Tiedau, J., Sansoni, L., Herrmann, H., Bartley, T.J., Silberhorn, C.: Limits on the heralding efficiencies and spectral purities of spectrally filtered single photons from photon-pair sources. Phys. Rev. A **95**, 061803 (2017) https://doi.org/10.1103/PhysRevA.95.061803

[26] Tsujimoto, Y., Ikuta, R., Wakui, K., Kobayashi, T., Fujiwara, M.: Quantum state tomography of qudits via hong-ou-mandel interference. Phys. Rev. Appl. **19**, 014008 (2023) https://doi.org/10.1103/PhysRevApplied.19.014008

[27] Wu, Q.-L., Namekata, N., Inoue, S.: High-fidelity entanglement swapping at telecommunication wavelengths. Journal of Physics B: Atomic, Molecular and Optical Physics **46**(23), 235503 (2013) https://doi.org/10.1088/0953-4075/46/23/235503

[28] Jin, R.-B., Takeoka, M., Takagi, U., Shimizu, R., Sasaki, M.: Highly efficient entanglement swapping and teleportation at telecom wavelength. Scientific Reports **5**(1), 9333 (2015) https://doi.org/10.1038/srep09333

[29] Tsujimoto, Y., Tanaka, M., Iwasaki, N., Ikuta, R., Miki, S., Yamashita, T., Terai, H., Yamamoto, T., Koashi, M., Imoto, N.: High-fidelity entanglement swapping and generation of three-qubit GHZ state using asynchronous telecom photon pair sources. Scientific Reports **8**(1), 1446 (2018) https://doi.org/10.1038/

s41598-018-19738-8

[30] Samara, F., Maring, N., Martin, A., Raja, A.S., Kippenberg, T.J., Zbinden, H., Thew, R.: Entanglement swapping between independent and asynchronous integrated photon-pair sources. Quantum Science and Technology **6**(4), 045024 (2021) https://doi.org/10.1088/2058-9565/abf599

[31] Wang, H., Yuan, H., Zeng, Q., Zhou, L., Ma, H., Yuan, Z.: High-rate cross-channel entanglement swapping between independent on-chip sources. Advanced Science **13**(9), 18802 (2026) https://doi.org/10.1002/advs.202518802

[32] Takeoka, M., Jin, R.-B., Sasaki, M.: Full analysis of multi-photon pair effects in spontaneous parametric down conversion based photonic quantum information processing. New Journal of Physics **17**(4), 043030 (2015) https://doi.org/10.1088/1367-2630/17/4/043030

[33] Seshadreesan, K.P., Takeoka, M., Sasaki, M.: Progress towards practical device-independent quantum key distribution with spontaneous parametric down-conversion sources, on-off photodetectors, and entanglement swapping. Phys. Rev. A **93**, 042328 (2016) https://doi.org/10.1103/PhysRevA.93.042328

[34] Tsujimoto, Y., You, C., Wakui, K., Fujiwara, M., Hayasaka, K., Miki, S., Terai, H., Sasaki, M., Dowling, J.P., Takeoka, M.: Heralded amplification of nonlocality via entanglement swapping. New Journal of Physics **22**(2), 023008 (2020) https://doi.org/10.1088/1367-2630/ab61da

[35] Morrison, C.L., Graffitti, F., Barrow, P., Pickston, A., Ho, J., Fedrizzi, A.: Frequency-bin entanglement from domain-engineered down-conversion. APL Photonics **7**(6), 066102 (2022) https://doi.org/10.1063/5.0089313

[36] Yamazaki, T., Ikuta, R., Kobayashi, T., Miki, S., China, F., Terai, H., Imoto, N., Yamamoto, T.: Massive-mode polarization entangled biphoton frequency comb. Scientific Reports **12**(1), 8964 (2022) https://doi.org/10.1038/s41598-022-12691-7

[37] Mazeas, F., Traetta, M., Bentivegna, M., Kaiser, F., Aktas, D., Zhang, W., Ramos, C.A., Ngah, L.A., Lunghi, T., Picholle, E., Belabas-Plougonven, N., Roux, X.L., Cassan, E., Marris-Morini, D., Vivien, L., Sauder, G., Labonté, L., Tanzilli, S.: High-quality photonic entanglement for wavelength-multiplexed quantum communication based on a silicon chip. Opt. Express **24**(25), 28731–28738 (2016) https://doi.org/10.1364/OE.24.028731

[38] Samara, F., Martin, A., Autebert, C., Karpov, M., Kippenberg, T.J., Zbinden, H., Thew, R.: High-rate photon pairs and sequential time-bin entanglement with si3n4 microring resonators. Opt. Express **27**(14), 19309–19318 (2019) https://doi.org/10.1364/OE.27.019309

[39] Cheng, R., Zhou, Y., Wang, S., Shen, M., Taher, T., Tang, H.X.: A 100-pixel photon-number-resolving detector unveiling photon statistics. Nature Photonics **17**(1), 112–119 (2023) https://doi.org/10.1038/s41566-022-01119-3

[40] Hao, H., Zhao, Q.-Y., Huang, Y.-H., Deng, J., Yang, F., Ru, S.-Y., Liu, Z., Wan, C., Liu, H., Li, Z.-J., Wang, H.-B., Tu, X.-C., Zhang, L.-B., Jia, X.-Q., Wu, X.-L., Chen, J., Kang, L., Wu, P.-H.: A compact multi-pixel superconducting nanowire single-photon detector array supporting gigabit space-to-ground communications. Light: Science & Applications **13**(1), 25 (2024) https://doi.org/10.1038/s41377-023-01374-1

[41] Cahall, C., Nicolich, K.L., Islam, N.T., Lafyatis, G.P., Miller, A.J., Gauthier, D.J., Kim, J.: Multi-photon detection using a conventional superconducting nanowire single-photon detector. Optica **4**(12), 1534–1535 (2017) https://doi.org/10.1364/OPTICA.4.001534

[42] Endo, M., Sonoyama, T., Matsuyama, M., Okamoto, F., Miki, S., Yabuno, M., China, F., Terai, H., Furusawa, A.: Quantum detector tomography of a superconducting nanostrip photon-number-resolving detector. Opt. Express **29**(8), 11728–11738 (2021) https://doi.org/10.1364/OE.423142

[43] Shapiro, J.H., Embleton, C., Raymer, M.G., Smith, B.J.: High-fidelity quasideterministic entanglement generation using phase-matched spectral islands in a zero-added-loss multiplexing architecture. Phys. Rev. A **112**, 062616 (2025) https://doi.org/10.1103/ykvm-17wh

[44] Mosley, P.J., Lundeen, J.S., Smith, B.J., Wasylczyk, P., U'Ren, A.B., Silberhorn, C., Walmsley, I.A.: Heralded generation of ultrafast single photons in pure quantum states. Phys. Rev. Lett. **100**, 133601 (2008) https://doi.org/10.1103/PhysRevLett.100.133601

METHODS

Simulation of the spectral purity-heralding efficiency trade-off

The spectral purity and the heralding efficiency of the photon pair in each DWDM channel is estimated by considering the joint spectral amplitude (JSA) of the biphoton state [44]. The biphoton state generated by SPDC is given by

$$|\Psi\rangle = \iint d\omega d\omega' \Phi(\omega, \omega') \hat{a}_s^\dagger(\omega) \hat{a}_i^\dagger(\omega') |\text{vac}\rangle, \tag{4}$$

where ω/ω' is an angular frequency of the signal/idler photon, $\Phi(\omega, \omega')$ is the JSA of the biphoton state, and $|\text{vac}\rangle$ is a vacuum state. $\hat{a}_{s/i}^\dagger(\omega)$ is the photon creation operator of the signal/idler photon whose angular frequency is ω. We consider the case where the signal and idler photons are separated into different spatial modes, and thus the commutation relation is given by $[\hat{a}_j(\omega), \hat{a}_k^\dagger(\omega')] = \delta_{jk}\delta(\omega - \omega')$ for $j, k \in \{s, i\}$.

The JSA is decomposed into $\Phi(\omega,\omega') = \alpha(\omega,\omega')\beta(\omega,\omega')$, where $\alpha(\omega,\omega')$ and $\beta(\omega,\omega')$ are the pump envelope function and the phase matching amplitude of the nonlinear crystal, respectively. Finally, filter functions $F_{s/i}(\omega)$ are applied to the JSA, yielding the filtered JSA $F_s(\omega)F_i(\omega')\Phi(\omega,\omega')$. The explicit forms of the pump envelope function $\alpha(\omega,\omega')$, the phase-matching amplitude $\beta(\omega,\omega')$, and the filter function $F_{s/i}(\omega)$ are approximated by

$$\alpha(\omega,\omega') = \mathrm{sech}\left(\frac{\omega+\omega'-\omega_p}{\Delta\sigma'_p}\right),$$
$$\beta(\omega,\omega') = \exp\left[-\frac{1}{2}\left(\frac{(\omega+\omega'-\omega_p)^2}{2(\Delta\sigma'_{\mathrm{pm}})^2}\right)^n\right],$$
$$F_{s/i}(\omega) = \exp\left[-\frac{1}{2}\left(\frac{\omega^2}{2(\Delta\sigma'_{\mathrm{f}})^2}\right)^m\right],$$

where $\Delta\sigma'_{\mathrm{p}}$, $\Delta\sigma'_{\mathrm{pm}}$, and $\Delta\sigma'_{\mathrm{f}}$ denote the width parameters corresponding to the measured FWHMs of $\Delta\sigma_p = 87\,\mathrm{GHz}$, $\Delta\sigma_{\mathrm{pm}} = 80\,\mathrm{GHz}$, and $\Delta\sigma_{\mathrm{f}} = 45\,\mathrm{GHz}$, respectively. Here, ω_p is the pump angular frequency, and $n = 1.4$ and $m = 2.5$ are the orders of the super-Gaussian functions. The heralding efficiency is given by the ratio of the two-fold coincidence probability to the single-detection probability, calculated as $\iint d\omega d\omega' |F_s(\omega)F_i(\omega')\Phi(\omega,\omega')|^2 / \iint d\omega d\omega' |F_s(\omega)\Phi(\omega,\omega')|^2 = 57\,\%$. The spectral purity was calculated from the singular-value decomposition (Schmidt decomposition) of the filtered JSA as $P := \sum_j \lambda_j^4 = 97\,\%$, where λ_j denotes the normalized jth Schmidt coefficient satisfying $\sum_j \lambda_j^2 = 1$. Fig. 1f was calculated by varying $\Delta\sigma_{\mathrm{pm}}$ while keeping $\Delta\sigma_p$ and $\Delta\sigma_f$ fixed. The validity of the simulation model is independently confirmed by the good agreement between the simulated and experimentally estimated spectral purity for the case where spectral filtering is applied only to the idler photons (see Supplementary Note 2 for details).

DATA AVAILABILITY

The authors declare that the data supporting the findings of this study are available within the paper, its supplementary information files, and Figshare.

ACKNOWLEDGEMENTS

This work was supported by Japan Society for the Promotion of Science (JP18K13487, JP20K14393, JP22K03490), JST FOREST Program (JPMJFR222V) and R&D of ICT Priority Technology Project (JPMI00316).

AUTHOR CONTRIBUTIONS

Y.T. and R.I. conceived the idea, Y.T. and K.W. designed the experimental setup. Y.T. and D.I. conducted the experiment with the assistance of K.W., Y.T. and D.I. analyzed the data and Y.T. performed the simulation. R.I. and K.W. contributed to the logical development and presentation of the work. K.W. developed and constructed

the electro-optic comb system. All authors contributed to discussions on the theory and experiment. Y.T. wrote the manuscript with the help of all the other authors.

COMPETING INTERESTS

The authors declare no competing interests.

Supplementary Files

This is a list of supplementary files associated with this preprint. Click to download.

- Supplementaryinformation.pdf